Bayesian parameter updating in linear structural dynamics with frequency transformed data using rational surrogate models

Felix Schneider[b], Iason Papaioannou[a], Daniel Straub[a], Christoph Winter[b], Gerhard Müller[b]

[a]*Engineering Risk Analysis Group, Technical University of Munich, Arcisstr. 21, 80333 Munich, Germany*
[b]*Chair of Structural Mechanics, Technical University of Munich, Arcisstr. 21, 80333 Munich, Germany*

Abstract

The identification of parameters of structural models through measurements of the system's response is of interest in many contexts. In Bayesian system identification the underlying inverse problem is formulated in a probabilistic setting, and Bayes' rule is applied to update a prior conjecture on the parameters. We apply the Bayesian framework to identify the parameters of structural systems using dynamic measurement data. The likelihood function is formulated in terms of the misfit of the frequency transformed data and the model frequency response function. We introduce a novel formulation that accounts for the correlation of the model error in both spatial and frequency domain. The proposed formulation is able to handle dense data sets in the frequency domain without need to manually select data points. Due to the high computational demands of sampling-based approaches for solving the Bayesian updating problem with expensive structural dynamics models, we resort to surrogate models. We apply a recently introduced rational surrogate model that approximates the complex frequency response as a rational of two polynomials with complex coefficients. Samples of the posterior distribution of the model parameters are then obtained through an adaptive sequential sampling approach using the surrogate instead of the original dynamic model. The proposed method is successfully applied to identify the orthotropic stiffness and damping parameters of a finite element model of a cross laminated timber plate.

Keywords: Bayesian Updating, Parameter Updating, Structural Dynamics, Surrogate Model, Frequency Response Function, Rational Function Approximation

1. Introduction

In structural dynamics, one is interested in determining the dynamic response of a structure or system as a basis for design decisions to ensure a satisfactory performance of the system related to safety and serviceability. Applications of structural dynamics have a wide range and include civil, automotive and aerospace engineering systems. The dynamic system response is governed by a set of differential equations, whose parameters define the structural characteristics of the system. Typically, the spatial domain is discretized by a numerical method, often the finite element method, in which case the problem is formulated as a discrete finite element system. The structural response can then be determined in the time or frequency domain.

When comparing computed model results to measurements conducted on existing structures, usually noticeable discrepancies are observed. These discrepancies are due to measurement errors and, more importantly, errors related to the model response. The latter stem from a lack of knowledge of the parameter values, such as the stiffness, damping or mass, and possibly a lack of understanding of the behavior of the actual system. The information contained in the measurements can be used to reduce these errors. This procedure is known as system identification [1, 2, 3, 4].

System identification can be performed with parametric and non-parametric approaches. This paper focuses on the parametric approach to model updating, also termed parameter updating or indirect system identification [5]. In the scope of parametric model updating, it is assumed that a mathematical model structure can be deduced from physical understanding of the structure. Then, the task is to determine the parameters of a chosen model such that the model best describes the measurements. A wide range of methods for parametric model updating have been proposed in the literature. Typically results from vibration measurements, such as acceleration time histories, frequency responses, natural frequencies and mode shapes, modal strains or curvatures or modal flexibilities [6] are utilized for this purpose. A distinction is made between deterministic and probabilistic approaches.

Deterministic approaches aim at finding an optimal parameter set, such that the discrepancy between model output and measurement is minimized. This is typically stated as an optimization problem. An overview of deterministic updating techniques can be found in [7]. Despite the fact that deterministic methods have been successfully applied, they have limitations. A common problem is the ill-posedness and ill-conditioning of the optimization problem. These issues can be efficiently treated through considering the inverse problem in a probabilistic framework.

Within a probabilistic framework, the quantities which are subject to uncertainty, such as parameters in the structural models and the errors themselves, are modeled as random variables. Commonly, the uncertainty is separated into model prediction and measurement uncertainty [6]. The uncertainty attributed to a quantity is then fully described by its probability density function (PDF). A commonly applied method to solve the probabilistic inverse problem is Bayesian updating. Through Bayesian updating the probabilistic description of the system parameters conditional on the observed measurements can be found [8]. The prior knowledge on the uncertain parameters, i.e. before the measurements become available, is expressed through the prior distribution. The distribution conditional on the measurements is found by application of Bayes' rule as the normalized product of the prior PDF and the likelihood function, which summarizes the measurements. The prior distribution imposes a regularization to the inverse problem, which effectively addresses its ill-posedness. The application of Bayesian methods to system identification is presented in, e.g., [9]. A Bayesian statistical framework for updating structural models is given by [10] and a detailed discussion of Bayesian methods in structural dynamics can be found in [11].

The evaluation of the posterior distribution requires solving a possibly high-dimensional integral. Except from some trivial cases this integral needs to be approximated numerically. A number of methods have been developed for this purpose. Asymptotic approximation methods, such as Laplace approximation [12], assume a Gaussian posterior distribution centered around the maximum a-posteriori (MAP) estimate [10]. Laplace approximations are inaccurate in problems with small numbers of measurements and are difficult to obtain in multimodal (non-uniquely identifiable) problems. For this reason, increasing attention has been given to stochastic methods, among which the most common method is Markov Chain Monte Carlo (MCMC) sampling [13]. A general discussion of MCMC sampling in the scope of Bayesian updating of structural models is given in [14]. Examples of MCMC methods and other variants thereof applied to Bayesian updating in structural dynamics include Gibbs-sampling [15], Transitional MCMC (TMCMC) [16, 17] or evolutionary MCMC methods [18, 19, 20]. An alternative approach to MCMC is the BUS approach, which employs sampling-based structural reliability methods to sample from the posterior distribution [21]. Application of the BUS approach combined with subset simulation to structural identification problems can be found in [21, 22, 23].

In sampling approaches, the model outcome needs to be computed for a large number of samples of the parameters, which can be prohibitive for computationally intensive models. For this reason, surrogate models are often used to approximate the computationally intensive model through a simple mathematical model that can be evaluated much faster. Popular choices include polynomial chaos expansions (PCE) [24, 25], Neumann series expansions [26] and machine learning techniques such as neural networks [27] or Gaussian process models [28]. Applications of surrogate modelling techniques combined with sampling approaches to Bayesian structural identification can be found in [29, 30]

Often, the inverse problem is formulated in terms of the modal properties of the system [15, 31, 32, 33, 34]. This requires the application of modal identification techniques, e.g., [35, 36, 37]. Despite the successful application and computational efficiency of modal data based approaches, the modal identification from time domain data can be error-prone. To avoid the modal analysis with possible identification errors, frequency response based approaches can be chosen. This is especially important for models with high modal density where modal identification is a challenging task [38]. It should be noted that the application of model updating based on the frequency response requires the availability of both, excitation and response measurement data.

Approaches to Bayesian updating using frequency response data are presented in [18, 19, 20, 39]. [19] discusses various error sources and their influence on the likelihood formulation. A PCE-based surrogate model is built to approximate the frequency response function (FRF) as a function of the modal properties. Posterior samples are computed through an evolutionary MCMC method. [39] solve the Bayesian identification problem with MCMC for a three degree of freedom system. Another approach is given in [40], where eigenfrequencies and FRF data are used in the updating procedure in low- and medium-frequency band, respectively.

This paper proposes a Bayesian parameter updating procedure for linear dynamic models that is based on frequency response data obtained from measurements. A novel formulation of the likelihood function relating the frequency data with the model response is introduced, which accounts for the correlation of the model error in both spatial and frequency domain. The formulation employs a multivariate complex normal distribution for the logarithm of the model error, leading to a joint normal distribution for the logarithm of the absolute value and the phase of the model error. The computational cost is reduced by combining the updating procedure with a surrogate model recently introduced in [41], which is especially suited for approximating FRFs. The surrogate model expresses the FRF as a ratio of polynomial chaos representations and is thus able to capture the highly non-linear behavior in terms of the model parameters. The coefficients of the surrogate model are determined based on a non-intrusive regression-based approach, which allows the coupling with any *black-box* finite element solver. We then employ an adaptive variant of BUS with subset simulation to generate samples from the posterior distribution [23] using the surrogate model instead of the numerical model of the system. A numerical example is presented that applies the proposed updating method to a cross-laminated timber (CLT) plate.

The outline of the paper is as follows. First, a description for the linear dynamic system with parameter uncertainty is given. In Section 3 the rational function approximation is introduced and a regression based method for estimating the coefficients is presented. Section 4 presents the Bayesian updating problem. Furthermore the likelihood function definition and the prior assumptions are discussed. Finally in Section 5, the proposed framework is applied to update the model parameters of a cross-laminated timber plate. The paper closes with the conclusions in Section 6.

2. Linear dynamic model with parameter uncertainty

Within the proposed framework, Bayesian updating makes use of measurement data to update the parameters of an engineering model of a given physical system. We assume that the physical system is modeled by a space-discretized, linear dynamic system with N degrees of freedom (DOF). Let $\mathbf{X}$ be a random vector with outcome space $\mathbb{R}^d$ and joint probability density function (PDF) $f_{\mathbf{X}}(\mathbf{x})$. $\mathbf{X}$ models a set of uncertain parameters that influence the state of the dynamic system. The matrices $\mathbf{K}(\mathbf{X})$, $\mathbf{C}(\mathbf{X})$ and $\mathbf{M}(\mathbf{X})$ denote stiffness, damping and mass matrix with parametric uncertainty. The equation of motion describing the system state in the frequency domain is given as

$$\mathbf{K}(\mathbf{X})\,\tilde{\mathbf{u}}(\omega,\mathbf{X}) + \mathrm{i}\omega\mathbf{C}(\mathbf{X})\,\tilde{\mathbf{u}}(\omega,\mathbf{X}) - \omega^2\mathbf{M}(\mathbf{X})\,\tilde{\mathbf{u}}(\omega,\mathbf{X}) = \tilde{\mathbf{f}}(\omega)\,. \tag{1}$$

Here, $\tilde{\mathbf{f}}(\omega)$ and $\tilde{\mathbf{u}}(\omega,\mathbf{X})$ are the deterministic force and the uncertain displacement vector in the frequency domain and $\mathrm{i} = \sqrt{-1}$ denotes the imaginary number.

From the above, it is evident that the outcome space of the solution $\tilde{\mathbf{u}}$ is the N-dimensional complex set $\mathbb{C}^N$. The frequency response function (FRF) $\tilde{h}_{ij} : \mathbb{R}\times\mathbb{R}^d \to \mathbb{C}$, defining the acceleration at DOF i due to a force $\tilde{f}_j$ at DOF j in terms of the circular frequency ω is then found by the ratio

$$\tilde{h}_{ij}(\omega,\mathbf{X}) = \frac{-\omega^2\tilde{u}_i(\omega,\mathbf{X})}{\tilde{f}_j(\omega)}. \tag{2}$$

3. Rational Function Approximation

Sampling-based Bayesian system identification requires a large number of model evaluations for different realizations of $\mathbf{X}$. Rather than using the model output directly, one may construct surrogate models that approximate the original model by a simple mathematical form. The surrogate model can then be used instead of the original model, thus alleviating high computational cost. A large number of surrogate models have been proposed in the literature, including artificial neural networks, polynomial chaos expansion (PCE) and Gaussian process models. The PCE is a popular choice due to its guaranteed convergence property [42]. However, as discussed in [41, 43], the classical PCE approach exhibits slow convergence in the case of representing FRFs due to their inherent nonlinear nature. In order to improve the convergence of PCE for representing FRFs, we introduced a non-intrusive rational surrogate model, termed rational function approximation, in [41]. This rational structure is suitable to represent FRFs in terms of the parameters of the model, as the original model itself can be interpreted as a rational function over the space of input parameters. We give a short but comprehensive summary of this model, which is subsequently applied in the probabilistic identification setting.

Without loss of generality, we assume that the random vector $\mathbf{X}$ follows the independent standard Gaussian distribution. In case this assumption does not apply it is possible to transform $\mathbf{X}$ to an equivalent independent standard normal random vector through an iso-probabilistic transform [44]. Consider a numerical model $\mathcal{M}(\mathbf{X})$ with outcome space $\mathbb{C}$. Let $P(\mathbf{X})$ and $Q(\mathbf{X})$ be truncated polynomial chaos representations with maximum orders m_p and m_q, such that

$$P(\mathbf{X}) = \sum_{i=0}^{n_p-1} p_i \Psi_i(\mathbf{X}), \qquad Q(\mathbf{X}) = \sum_{i=0}^{n_q-1} q_i \Psi_i(\mathbf{X}). \tag{3}$$

Here $\{p_i \in \mathbb{C}, i = 0, \ldots, n_p - 1\}$ and $\{q_i \in \mathbb{C}, i = 0, \ldots, n_q - 1\}$ are complex coefficients and Ψ_i are the multivariate Hermite polynomials. The set $\{\Psi_i, i = 0, \ldots, n\}$ consists of products of univariate normalized Hermite polynomials of maximum total degree m; it is $n = \binom{d+m}{m}$. We define the rational function approximation (RFA) $R(\mathbf{X})$ obtained by taking the ratio of the two PCE representations of Eq. (3):

$$R(\mathbf{X}) = \frac{P(\mathbf{X})}{Q(\mathbf{X})} = \frac{\sum_{i=0}^{n_p-1} p_i \Psi_i(\mathbf{X})}{\sum_{i=0}^{n_q-1} q_i \Psi_i(\mathbf{X})}. \tag{4}$$

In order to determine the unknown coefficients in Eq. (4), a regression method is developed in [41]. In this approach the coefficients are found by minimization of the modified mean-square error $\widetilde{\mathrm{err}}$, defined as

$$\widetilde{\mathrm{err}} = \mathrm{E}\left[|\mathcal{M}(\mathbf{X})\, Q(\mathbf{X}) - P(\mathbf{X})|^2\right]. \tag{5}$$

$\widetilde{\mathrm{err}}$ is the mean-square of the truncation error $\mathcal{M}(\mathbf{X}) - R(\mathbf{X})$ multiplied by the denominator $Q(\mathbf{X})$ of the rational approximation. Using a set of samples $\{\mathbf{x}_k, k = 1, \ldots, N\}$ of $\mathbf{X}$ and corresponding model evaluations $\{\mathcal{M}(\mathbf{x}_k), k = 1, \ldots, N\}$, we estimate the coefficients $\{p_i\}$ and $\{q_i\}$ through minimizing a sample estimate of $\widetilde{\mathrm{err}}$. Throughout this paper, we use Latin hypercube sampling (LHS) in order to generate samples of $\mathbf{X}$. Substituting the expressions of Eq. (3) in Eq. (5) and performing the sampling approximation, we define the following minimization problem

$$\{\mathbf{p}, \mathbf{q}\} = \underset{\{\tilde{\mathbf{p}}, \tilde{\mathbf{q}}\} \in \mathbb{C}^{n_p+n_q}}{\arg\min} \frac{1}{N} \sum_{k=1}^{N} \left| \mathcal{M}(\mathbf{x}_k) \sum_{i=0}^{n_q-1} \tilde{q}_i \Psi_i(\mathbf{x}_k) - \sum_{i=0}^{n_p-1} \tilde{p}_i \Psi_i(\mathbf{x}_k) \right|^2. \tag{6}$$

The minimizer is the solution of the following homogeneous linear system of equations of dimensions $(n_p + n_q) \times (n_p + n_q)$

$$\mathbf{A}\mathbf{r} = \mathbf{0}. \tag{7}$$

Here $\mathbf{r} = [\mathbf{p}; \mathbf{q}] \in \mathbb{C}^{(n_p+n_q)}$ is the vector of unknown coefficients and $\mathbf{A} \in \mathbb{C}^{(n_p+n_q)\times(n_p+n_q)}$ is defined as follows

$$\mathbf{A} = \begin{bmatrix} \boldsymbol{\Psi}_P^T \boldsymbol{\Psi}_P & -\boldsymbol{\Psi}_P^T \operatorname{diag}(\mathbf{M})\, \boldsymbol{\Psi}_Q \\ -\boldsymbol{\Psi}_Q^T \operatorname{diag}(\mathbf{M}^*)\, \boldsymbol{\Psi}_P & \boldsymbol{\Psi}_Q^T \operatorname{diag}(\mathbf{M} \circ \mathbf{M}^*)\, \boldsymbol{\Psi}_Q \end{bmatrix}, \tag{8}$$

where $\operatorname{diag}(\cdot)$ is the diagonal matrix whose diagonal entries are the elements of $(\cdot)$, $\circ$ denotes the Hadamard product and $*$ denotes complex conjugation. Matrices $\boldsymbol{\Psi}_P \in \mathbb{R}^{N\times n_p}$ and $\boldsymbol{\Psi}_Q \in \mathbb{R}^{N\times n_q}$ have as (i, j)-element $\Psi_j(\mathbf{x}_i)$ and vector $\mathbf{M} \in \mathbb{C}^N$ has as i-element the model evaluation $\mathcal{M}(\mathbf{x}_i)$. A non-trivial solution $\mathbf{r} \neq \mathbf{0}$ to the homogeneous system of Eq. (7) can be found through the minimum-norm least-squares solution.

$$r = \underset{\widehat{\mathbf{r}} \in \mathbb{C}^{(n_p+n_q)}}{\arg\min} \left\| \mathbf{A}\widehat{\mathbf{r}} \right\|_2 \text{ subject to } \left\| \widehat{\mathbf{r}} \right\|_2 = 1. \tag{9}$$

A solution to this problem can be found through applying singular value decomposition.

4. Bayesian parameter updating with FRF data

Bayesian updating (also termed Bayesian inference) is a statistical framework that can be used to infer model parameters and their uncertainty based on measurements. Consider a set of measurements of a dynamic system $\mathcal{Y}_O$ are available, from which the frequency response can be obtained. $\mathcal{Y}_O$ could include data obtained at different frequencies and spatial locations of the structure. The measurements $\mathcal{Y}_O$ can be used to learn the probability distribution of the model parameters $\mathbf{X}$ by application of Bayes' theorem, which states

$$f_{\mathbf{X}}(\mathbf{x}|\mathcal{Y}_O) = c_E^{-1} L(\mathbf{x}|\mathcal{Y}_O) f_{\mathbf{X}}(\mathbf{x}) \ . \tag{10}$$

Here $f_{\mathbf{X}}(\mathbf{x})$ denotes the prior joint PDF of the model parameters, i.e. the joint PDF of $\mathbf{X}$ before the measurements $\mathcal{Y}_O$ become available, $f_{\mathbf{X}}(\mathbf{x}|\mathcal{Y}_O)$ is the posterior joint PDF of $\mathbf{X}$, i.e. the conditional PDF of $\mathbf{X}$ given $\mathcal{Y}_O$, and $L(\mathbf{x}|\mathcal{Y}_O)$ is the likelihood function describing the information in $\mathcal{Y}_O$. $L(\mathbf{x}|\mathcal{Y}_O)$ is proportional to the probability of $\mathcal{Y}_O$ given a parameter state, i.e.

$$L(\mathbf{x}|\mathcal{Y}_O) \propto \Pr(\mathcal{Y}_O|\mathbf{X} = \mathbf{x}) \ . \tag{11}$$

The constant c_E is a proportionality constant that ensures that the posterior PDF integrates to 1. It is:

$$c_E = \int_{\Omega} L(\mathbf{x}|\mathcal{Y}_O) f_{\mathbf{X}}(\mathbf{x}) \ \mathrm{d}\mathbf{x} \ , \tag{12}$$

where $\Omega \subseteq \mathbb{R}^d$ is the outcome space of the prior PDF of $\mathbf{X}$. c_E is a measure of the plausibility of the assumed model class and is often referred to as model evidence [45]. The model evidence gives a rational means for selecting the most appropriate model to describe the data $\mathcal{Y}_O$, as the model that maximizes c_E among the considered models. In the following, we derive the likelihood function that describes measurements of the FRF of a dynamic system through relating the measurement outcome with the response of the surrogate model.

4.1. Likelihood function

The likelihood function is derived by considering the relation between the response of the surrogate model and the measurement outcomes. We assume an error model that relates the surrogate model and measurement FRFs as follows

$$\mathcal{Y}_O + \boldsymbol{\varepsilon}_o = \mathcal{Y}_S(\mathbf{X}) \circ \boldsymbol{\varepsilon}_{\mathcal{M}} \,, \tag{13}$$

where $\mathcal{Y}_O \in \mathbb{C}^{no}$ is the measurement data, $\mathcal{Y}_S \in \mathbb{C}^{no}$ is the surrogate model outcome, $\boldsymbol{\varepsilon}_o$ and $\boldsymbol{\varepsilon}_{\mathcal{M}}$ are the observation and model error, respectively, which we model as random variables, and $\circ$ denotes the Hadamard product. All quantities denote vector quantities. The model error collects all errors that are introduced, e.g., through mathematical modelling of a system, the numerical discretization and the surrogate approximation. The model errors are often assumed to be multiplicative, see, e.g., [21]. The additive observation error can stem from noise contributions from the measurement setup or Fourier transform errors. We make the assumption that the observation error is negligible compared to the model error, hence we set $\boldsymbol{\varepsilon}_o = \mathbf{0}$. This assumption is consistent with the application we consider in Section 5. In the following we set $\boldsymbol{\varepsilon} = \boldsymbol{\varepsilon}_{\mathcal{M}}$ for notational convenience. The model errors can be expressed as follows:

$$\boldsymbol{\varepsilon} = |\boldsymbol{\varepsilon}| \mathrm{e}^{\mathrm{i}\boldsymbol{\theta}} \,, \tag{14}$$

where $|\varepsilon|$ denotes the amplitudes and $\boldsymbol{\theta}$ the phases of the model errors. We model the amplitudes $|\boldsymbol{\varepsilon}|$ with a multivariate lognormal distribution and the phases $\boldsymbol{\theta}$ with a multivariate normal distribution and assume independence between $|\boldsymbol{\varepsilon}|$ and $\boldsymbol{\theta}$. This implies that the element-wise natural logarithm of $\boldsymbol{\varepsilon}$,

$$\log \boldsymbol{\varepsilon} = \log |\boldsymbol{\varepsilon}| + \mathrm{i}\boldsymbol{\theta} \,, \tag{15}$$

follows the improper multivariate complex normal distribution [46]. Taking the logarithm of Eq. (13), we get:

$$\log \mathcal{Y}_O = \log \mathcal{Y}_S(\mathbf{X}) + \log \boldsymbol{\varepsilon} \,. \tag{16}$$

This leads to the following expression for the likelihood function:

$$L(\mathbf{x}|\mathcal{Y}_O) = f_{\log \boldsymbol{\varepsilon}}(\log \mathcal{Y}_O - \log \mathcal{Y}_S(\mathbf{x})) \tag{17}$$

The complex normal distribution can be expressed in terms of a joint normal distribution for real and imaginary part. For notational convenience we define $\mathbf{w} = \log|\boldsymbol{\varepsilon}|$. Thus, the real composite random vector $[\mathbf{w}; \boldsymbol{\theta}]$ follows the normal distribution. We finally obtain

$$\begin{bmatrix} \mathbf{w} \\ \boldsymbol{\theta} \end{bmatrix} \sim \mathcal{N}\left(\begin{bmatrix} \mathbf{0} \\ \mathbf{0} \end{bmatrix}, \begin{bmatrix} \sigma_w^2 \mathbf{R}_w & \mathbf{0} \\ \mathbf{0} & \sigma_\theta^2 \mathbf{R}_\theta \end{bmatrix} \right), \tag{18}$$

where σ_w is the global standard deviation of the magnitude of the model error, σ_θ is the global standard deviation of the phase of the model error, and $\mathbf{R}_w$ and $\mathbf{R}_\theta$ are the correlation coefficient matrices. Under this model, it is necessary to specify a correlation model for $\mathbf{R}_w$ and $\mathbf{R}_\theta$. For the remainder of this paper we assume that $\mathbf{R}_w$ and $\mathbf{R}_\theta$ are equal and set $\mathbf{R} = \mathbf{R}_w = \mathbf{R}_\theta$. A straightforward choice would be to neglect correlation between observations and to use the identity matrix, $\mathbf{R} = \mathbf{I}$. However, the prediction error correlation can have significant influence on the posterior distribution, especially when densely populated sensor grids and high sampling rates are used [47]. In Section 5 we compare the results obtained using the below introduced correlation model and the case when the correlation of the model error is neglected. The following stationary exponential correlation model is chosen to model the dependency between spatial observation points and frequency domain points:

$$\rho\left(\Delta_z, \Delta_f\right) = r \cdot \rho_f\left(\Delta_f\right) + (1 - r) \cdot \rho_z\left(\Delta_z\right), \tag{19}$$

with

$$\rho_z\left(\Delta_z\right) = \exp\left(-\frac{\Delta_z}{l_{\mathrm{co},z}}\right), \tag{20}$$

$$\rho_f\left(\Delta_f\right) = \exp\left(-\frac{\Delta_f}{l_{\mathrm{co},f}}\right), \tag{21}$$

and $\Delta_z = \left\|\mathbf{z}_i - \mathbf{z}_j\right\|_2$ being the euclidean distances between the accelerometer locations $\mathbf{z}_i$ and $\mathbf{z}_j$, $l_{\mathrm{co},z}$ the corresponding spatial correlation length, $\Delta_f = \left|f_i - f_j\right|$ the absolute difference between two frequency points f_i and f_j and $l_{\mathrm{co},f}$ the corresponding frequency domain correlation length. The ratio $r \in [0, 1]$ models the split between the spatial and frequency domain correlation. In contrast to multiplying both univariate correlation models, the additive link allows for a basic correlation in either of the limits

$$\lim_{\Delta_f \to \infty} \rho = (1 - r)\rho_z\left(\Delta_z\right), \tag{22}$$

$$\lim_{\Delta_z \to \infty} \rho = r\rho_f\left(\Delta_f\right). \tag{23}$$

Still, it holds $\lim\limits_{\Delta_f, \Delta_z \to \infty} \rho = 0$. Measurement and surrogate model evaluations are arranged in vector format and ordered according to the index

$$l = i + (s - 1) \cdot n_{\mathrm{mp}}, \tag{24}$$

where i is an index over all accelerometer points n_{mp} and s over all frequency points n_f. For simplicity we assume a single observation at each point in space and frequency domain $(\mathbf{z}_i, f)$. Thus, the number of observations becomes $n_O = n_{\mathrm{mp}} \cdot n_f$. The correlation coefficient matrix $\boldsymbol{R}$ then reads

$$\mathbf{R} = r\left(\mathbf{R}_{ff} \otimes \mathbf{I}_{n_{\mathrm{mp}}}\right) + (1 - r)\left(\mathbf{I}_{n_f} \otimes \mathbf{R}_{zz}\right), \tag{25}$$

with $\mathbf{I}_n$ the $n \times n$-identity matrix, $\mathbf{R}_{zz}$ the $n_{\mathrm{mp}} \times n_{\mathrm{mp}}$ spatial correlation matrix based on Eq. (20), $\mathbf{R}_{ff}$ the $n_f \times n_f$ frequency domain correlation matrix based on Eq. (21), and $\otimes$ the Kronecker-product. Thus, $\boldsymbol{\mu}_{\boldsymbol{\varepsilon}}$ and $\boldsymbol{\Sigma}_{\boldsymbol{\varepsilon}}$ have size $2n_O \times 1$ and $2n_O \times 2n_O$, respectively.

In total, the model error is now described by five hyper-parameters: model error standard deviations σ_w and σ_θ, spatial correlation length $l_{\mathrm{co},z}$, frequency correlation length $l_{\mathrm{co},f}$ and ratio r. Since there are no reliable assumptions on those quantities, they are also treated as unknown random variables and included in the updating scheme.

The joint PDF of real and imaginary part of the model error for a complex scalar observation assuming the joint lognormal-normal model for absolute value and phase is depicted in Fig. 1 for different combinations of standard

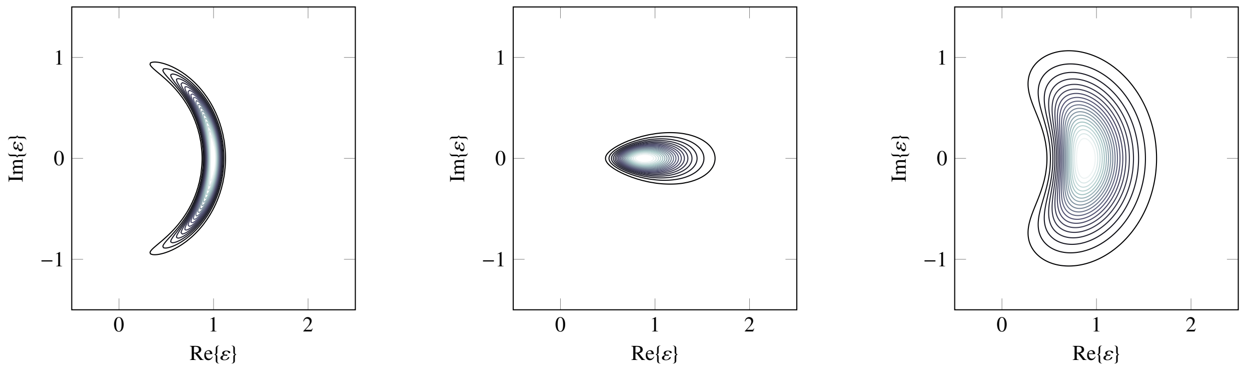

(a) $\sigma_w = 0.1$, $\sigma_\theta = 0.5$ (b) $\sigma_w = 0.5$, $\sigma_\theta = 0.1$ (c) $\sigma_w = 0.5$, $\sigma_\theta = 0.5$

Figure 1: Contour plot of the joint PDF of the real and imaginary part of the (scalar) complex model error, $\mathrm{Re}\{\varepsilon\}$ and $\mathrm{Im}\{\varepsilon\}$, under the assumption of lognormally distributed absolute value $|\varepsilon|$ and normally distributed phase θ for different combinations of standard deviations σ_w and σ_θ, as defined in Eq. A.9. It can be observed that through the proposed error model the likelihood functions gets a directional characteristic which points away from the origin of the complex plane.

deviations of the logarithm of the absolute value and the phase of the error σ_w and σ_θ, respectively. We derive the joint PDF of real and imaginary parts in Appendix A. The illustration of real and imaginary part offers an insight into the structure of the model error under the proposed assumptions. One can observe that the shape of the joint PDF changes significantly with σ_w and σ_θ. For a low standard deviation of the logarithm of the absolute value, most of the probability mass lies along a circular arc, the median absolute value is equal to one. The spread of the joint PDF along $\mathrm{Im}\{\epsilon\}$ is controlled by the standard deviation of the phase σ_θ. For a low standard deviation of the phase, most of the probability lies along the real line. In the case where both standard deviations are significant, we observe that the contours of the joint PDF align along a kidney-like shape. In the vicinity of the origin of the complex plane the joint PDF assumes low values, which is due to the fact the error is assumed to be multiplicative. One always obtains a directional characteristic whereby the probability mass points away from the origin of the complex plane.

Remark: Although we neglect the additive error in the derivation it can be easily incorporated when applying sampling-based approaches for updating. If one assumes a complex normal distribution for the additive error, this can be done through adding noise samples from the additivie error to the measurement observation. This approach enables learning the variance hyperparamter of the additive noise.

4.2. Bayesian updating with subset simulation

The solution of Eq. (10) requires evaluating a potentially high-dimensional integral. Here, we apply a sampling-based approach to approximate the posterior distribution and estimate the model evidence c_E that combines the BUS approach with subset simulation (SuS). The BUS approach, originally proposed in [21], is based on redefining the Bayesian updating problem as a structural reliability problem. Consider the augmented outcome space $[\mathbf{x}, p]$, where $\mathbf{x}$ represents outcomes of the random vector with density equal to the prior density $f_{\mathbf{X}}(\mathbf{x})$ and p is the outcome of a standard uniform random variable that is independent from $\mathbf{X}$. In structural reliability, one is interested in evaluating the probability of failure of a structure. The failure event is described in terms of a limit-state function, $h(\mathbf{x}, p)$, as the collection of outcomes for which $h(\mathbf{x}, p) \leq 0$. Consider the limit-state function:

$$h(\mathbf{x}, p) = p - cL(\mathbf{x}|\mathcal{Y}_O) \ , \tag{26}$$

where c is a constant that satisfies $cL(\mathbf{x}|\mathcal{Y}_O) \leq 1$ for all $\mathbf{x} \in \Omega$. It can be shown that the posterior PDF can be retrieved by censoring the prior PDF $f_{\mathbf{X}}(\mathbf{x})$ on the domain $\Omega_Z = \{h(\mathbf{x}, p) \leq 0\}$ [21]. Therefore samples from the posterior distribution can be obtained as the failure samples in the structural reliability problem for evaluating $\Pr(Z)$ with $Z = \{[\mathbf{x}, p] \in \Omega_Z\}$. If the likelihood function is concentrated around small areas of Ω (i.e. the likelihood is peaky), then the probability $\Pr(Z)$ becomes small and standard Monte Carlo is inefficient. Therefore, alternative structural reliability methods are used that are able to estimate small failure probabilities more efficiently.

Here, we apply SuS, which is an adaptive Monte Carlo method developed for estimation of small failure probabilities in high dimensions [48]. The basic idea of SuS is to express the event Z as an intersection of a set of intermediate nested events, i.e. $Z = \cap_{i=1}^{J} Z_i$ with $Z_0 \supset Z_1 \supset \cdots \supset Z_J = Z$ and Z_0 representing the certain event. The probability $\Pr(Z)$ is then expressed as a product of conditional probabilities:

$$\Pr(Z) = \Pr\left(\cap_{i=1}^{J} Z_i\right) = \prod_{i=1}^{J} \Pr(Z_i|Z_{i-1}) \,. \tag{27}$$

The first probability $\Pr(Z_1|Z_0) = \Pr(Z_1)$ is evaluated with standard Monte Carlo. Then MCMC approaches are used to sequentially estimate the conditional probabilities $\Pr(Z_i|Z_{i-1}), i = 2, \ldots, J$ [49]. In the final sampling step, an additional MCMC step is applied to obtain failure samples conditional on $Z_J = Z$, which follow the posterior distribution. We employ an adaptive version of the BUS-SuS approach, proposed in [23], which adaptively estimates the constant c in Eq. (26) as the reciprocal of the maximum over the likelihood function values for all samples. Having estimated the probability $\Pr(Z)$ and constant c, an estimate of the model evidence c_E is obtained as:

$$\hat{c}_E = \frac{\widehat{\Pr}(Z)}{\hat{c}} \,. \tag{28}$$

Details on the implementation of the adaptive BUS-SuS approach can be found in [23]. Throughout this paper, we set the intermediate conditional probabilities to $p_0 = 0.2$. The number of samples per level and posterior samples is chosen to be $N_b = 5 \cdot 10^4$.

5. Application

The proposed method is applied to measurements and model of a cross-laminated timber (CLT) plate, depicted in Fig. 2. CLT is a novel timber building material made of perpendicularly glued timber beams [50]. The model updating problem for the bending vibration properties of CLT was also approached by [51], where model updating was done for stripes of CLT, thus neglecting the two-dimensional behavior of plate elements. Therein, modal data is used to identify material parameters and investigate homogenized and sandwich models.

In the following, we first discuss specific aspects of the mechanical modeling of CLT and describe the evaluation of the measurements. Subsequently, we introduce the prior PDF and then investigate the proposed updating method. The frequency range from 25 to 160 Hz is considered, and uniformly sampled frequencies are used with a frequency step size of 1 Hz. For the calculation of the coefficients of the rational approximation in Eq. (4), we use a maximum polynomial degree of $m_p = 3$ and $m_q = 4$ for numerator and denominator, respectively. The experimental design used to identify the parameters of the surrogate model is generated with LHS from the prior distribution of the input random variables. The size of the experimental design N is chosen as three times the number of unknown coefficients $n_p + n_q$.

5.1. Finite element models of the cross-laminated timber plate

In Section 2, the general linear structural dynamics problem is presented. Here, structural matrices $\mathbf{K}(\mathbf{X})$, $\mathbf{C}(\mathbf{X})$ and $\mathbf{M}(\mathbf{X})$ enter. These depend, inter alia, on the underlying governing equations. Various approaches can be chosen to mechanically model the dynamic behavior of CLT structures. We investigate two alternatives, one applying Reissner-Mindlin shell theory using homogenized material parameters, as described in [52], and the other derived from three-dimensional elasticity theory, where each layer volume is modeled separately. For both models an orthotropic material model is applied, which is described by nine parameters, namely three Young's moduli, three shear moduli and three Poisson's ratios (cf. [52]). All layers are assigned the same stiffness values, i.e. all material parameters are constant throughout the plate domain. The cross-wise layering is accounted for by considering the local fiber directions in each layer. From here on the models are termed shell and solid model, respectively. Both models are implemented in the commercial finite element software ANSYS® [53], using the element formulations SHELL281 for the shell model and SOLID 185 for the solid model. For both models a spatial mesh size of $h = 0.1$ m in the finite element analysis is used. We further choose a linear hysteretic damping model, as it supports a frequency-independent energy loss for steady state motion per cycle, which is a realistic assumption for many materials, including cross-laminated timber [54]. Under this model, the damping matrix can be expressed through

$$\mathbf{C} = \frac{\eta}{|\omega|}\mathbf{K}\,. \tag{29}$$

Here, η is the hysteretic or structural damping coefficient, which is related to the damping ratio ζ as $\eta = 2\zeta$.

5.2. Measurement

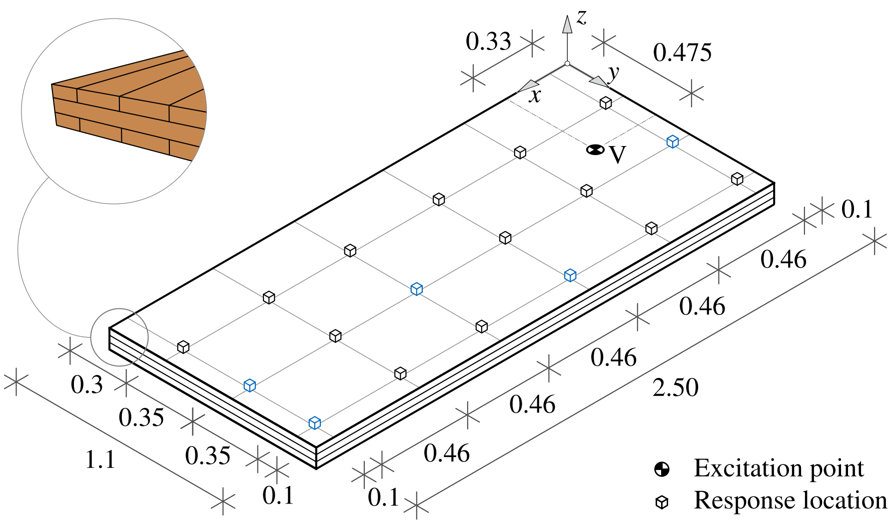

Figure 2: Geometry and setup of CLT-element, all measures in m. The five accelerometers depicted in blue (—) are highlighted for clarity, as we use data obtained at these locations.

Measurements for the investigations in this paper were available from the University of Applied Sciences in Rosenheim [55]. The plate under consideration consists of three cross wise laminated layers of timber with a thickness of $t_i = 0.027$ m (total thickness $t = 0.081$ m), length of $l = 2.5$ m and breadth of $b = 1.1$ m, as depicted in Fig. 2. The plate is hanging freely from two cables attached at the boundary $x = 0$. Excitation is applied using an impedance hammer to create an impulse force at forcing location V. The input force and response acceleration time histories are recorded at 18 spatial locations on the depicted grid. Each accelerometer is associated with a tupel (j, k) that describes its placement on the plate in x- and y-direction. Indices j and k are ordered in increasing x- and y-direction, respectively. Thus, $j \in \{1, \ldots, 6\}$ and $k \in \{1, \ldots, 3\}$. A single index is given by $i = j + 6\,(k - 1)$ with $i \in \{1, \ldots, 18\}$ for the $n_{\mathrm{mp}} = 18$ accelerometer positions. The response is measured perpendicular to the plate surface. A measurement time of $T = 16$ s and sampling frequency of $f_S = 19200$ Hz are used and the measurement is repeated five times. Subsequently, a Fast Fourier Transform (FFT) is applied to obtain frequency domain data. As the signals are transients, and decay within the measurement time, we do not apply windowing to the signal. The corresponding Nyquist frequency follows as $\frac{f_S}{2} = 9600$ Hz (cf. [56]). From the Fourier transformed data we evaluate the experimental frequency response function using the H1-estimator, see e.g. in [4]. As an example, the resulting estimate of the absolute value of the frequency response from measurement point $(j, k) = (6, 3)$ as well as the individual FRFs obtained from the five repetitions are depicted in Fig. 3 in the frequency range from 0 to 300 Hz. It can be observed that above approximately 160 Hz, there are inconsistencies between the individual measurements (grey dashed lines). For this reason we restrict the considered frequency range to a maximum frequency of 160 Hz. Furthermore, after careful investigation of the measurement data, we choose the locations with a coherence (cf. [4]) close to one throughout the whole frequency range of interest. The results for $k = 1$ showed poor coherence, thus we did not include any of these points. This leads to five points ($i \in \{7, 10, 12, 14, 18\}$), indicated in blue in Fig. 2.

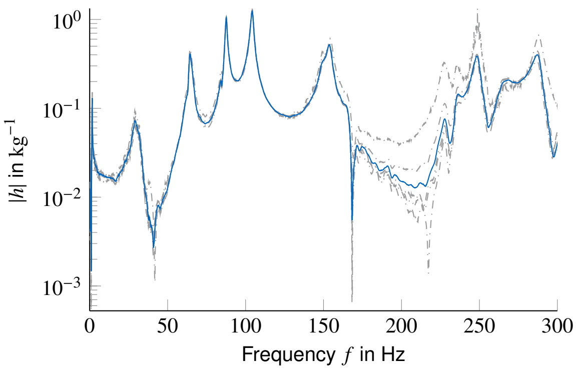

Figure 3: Experimental frequency response function for CLT plate; load point V; accelerometer $(j, k) = (6, 3)$, $i = 18$; (—) H1 estimator of FRF, $(\cdots)$ individual FRFs obtained seperately from each measurement by dividing the frequency transforms.

5.3. Prior distribution

The vector of random variables is

$$\mathbf{X} = \left[E_x, E_y, G_{xy}, \zeta, \sigma_w, \sigma_\theta, l_{\text{co},z}, l_{\text{co},f}, r\right]^T . \tag{30}$$

Here E_x and E_y are the Youngs's moduli in longitudinal direction and cross-direction, respectively, G_{xy} is the in-plane shear modulus and ζ is the damping ratio. The Young's modulus in the third direction E_z (the thickness direction) has no influence on the response unless the excitation frequency reaches the eigenfrequency of the first thickness mode, which can be neglected here [57]. For this reason we insert it deterministically as $3.7 \cdot 10^8$. Furthermore, we consider the out-of-plane shear moduli in longitudinal and cross-direction, G_{xz} and G_{yz}, as deterministic and do not include them in the updating. Initial investigations show that their distributions are not well-identifiable. This is related to their low influence on the model outcome in the considered frequency range. For those frequencies the shear deformations can be considered to be negligible and the Kirchhoff assumption should hold valid. This is further indicated when comparing the wave length and speed for waves in homogeneous orthotropic media, as the deviations in these quantities, assuming Kirchhoff or Reissner-Mindlin theory, are quite small. The minor Poisson's ratios and material density are modeled deterministically as $\nu_{yx} = \nu_{zx} = 1.4 \cdot 10^{-2}$, $\nu_{zy} = 0.3$ and $\rho = 442 \frac{\text{kg}}{\text{m}^3}$. The density is calculated from the measured total weight of the plate. A global damping ratio is assumed, whose prior distribution is based on engineering judgment. The prior distribution assumptions for the stiffness parameters are separately discussed for solid and shell model subsequently. The model choices are summarized in Tab. 1.

5.3.1. Solid model

For the solid model, the stiffnesses are given with respect to the local orientation of the single layers and the single layers are all modeled by a single stiffness value. The mean values of the material properties for the single layers are taken from [58]. The coefficient of variation and distribution type of the single layer properties are chosen in accordance with [59]. The coefficients 0.85 and 0.7 for E_y and G_{xy}, respectively, account for missing gluing on narrow edges in cross direction and are taken from [60].

5.3.2. Shell model

The prior distribution assumptions of the homogenized material parameters are obtained as follows. First mean values of the material properties for the single layers are taken from [58]. Subsequently, these are propagated through the homogenization model given in [52] to obtain the corresponding homogenized material parameters. These can thus be seen as first-order approximations of the true mean values of the homogenized material properties. The homogenized Young's moduli of the shell model can be interpreted as the weighted arithmetic mean of the single layers' Young's moduli. Due to the different orientation we observe a more significant difference between the Young's moduli for shell and solid model in y-direction as compared to the Young's moduli in x-direction. The coefficient of variation and distribution type of the homogenized properties are chosen in accordance with [59]. Note that [58, 59]

Table 1: Parameters for prior distributions for shell and solid model

	Distribution	Mean value		Coefficient of variation
		Shell model	Solid model	
E_x in Nm^{-2}	Lognormal	$1.061 \cdot 10^{10}$	$1.1 \cdot 10^{10}$	0.1
E_y in Nm^{-2}	Lognormal	$0.85 \cdot 7.605 \cdot 10^8 = 6.5 \cdot 10^8$	$0.85 \cdot 3.667 \cdot 10^8 = 3.1 \cdot 10^8$	0.1
G_{xy} in Nm^{-2}	Lognormal	$0.7 \cdot 6.9 \cdot 10^8 = 4,83 \cdot 10^8$		0.1
ζ	Lognormal	$2 \cdot 10^{-2}$		0.3
σ_w	Lognormal	0.1		1
σ_θ	Lognormal	0.1		1
$l_{\mathrm{co},z}$ in m	Lognormal	0.5		1
$l_{\mathrm{co},f}$ in Hz	Lognormal	5		1
	Distribution	Lower bound		Upper bound
r	Uniform	0		1

give guidelines for choosing distributions of materials of single layers; we assume that these still hold well enough after homogenization. This is consistent with the prior distributions of the solid model, where the material parameters at each layer are assumed to be fully correlated. The coefficients 0.85 and 0.7 for E_y and G_{xy}, respectively, account for missing gluing on narrow edges in cross direction and are taken from [60]. We emphasize that the Young's moduli represent the individual layer's material characteristics for the solid model while for the shell model they represent the overall plate's homogenized orthotropic material parameters.

5.3.3. Error model

The prior distribution of the error model hyperparameters are chosen based on the authors' judgement. We choose large values for the prior coefficients of variation in order to make the prior distributions less informative.

5.4. Results

In the following, we present results for both models. FE model evaluations are done for the chosen n_f frequency points, and one surrogate model is built for each combination of location and frequency point. Thus, $n_O = 5 \cdot 136 = 680$ surrogate models are built. For the generated surrogate models, the relative 4-fold cross-validation error, as defined in [41], is depicted in Fig. B.9 in Appendix B. The cross-validation error is evaluated using the N experimental design samples. Low error measures are obtained throughout the spatial and frequency range except for few points. It is expected that these errors are not significant as long as the posterior probability mass is not too far off the prior sample range, since these large errors are caused by outliers in the experimental design [41].

Estimates of the posterior distribution parameters are summarized in Tab. 2 and scatter plots of the $N_b = 5 \cdot 10^4$ posterior samples are shown in Figs. 4 and 5 for the shell and solid model, respectively. Figs. 8 shows the posterior samples for the shell model in the case, where the model error correlation is neglected.

Both elastic moduli E_x and E_y are identified with a high degree of certainty as indicated by the low posterior coefficients of variation. For the shell model, the posterior coefficient of variation of E_y is 0.3%, which is lower than the value 0.9% obtained with the solid model. We note that the results for shell and solid model are different due to the underlying homogenization of the material parameters for the shell model. Also the in-plane shear modulus G_{xy} is well-identified. This observation holds for both models. The posterior mean values for the damping parameter ζ are similar for both models and are slightly increased relative to the prior mean value; they now have smaller coefficient of variation compared to the prior distribution.

The posterior mean values of the model error standard deviations σ_w and σ_θ are larger than the prior mean values. Furthermore, the posterior mean values of both correlation lengths are increased. They show very good agreement for both models. The mean value of the spatial correlation length $l_{\mathrm{co},z}$ lies well above the physical dimensions of the plate, implying highly correlated model errors in the spatial domain. One can observe that the posterior distribution

Table 2: Mean, mode and coefficient of variation of posterior distribution.

	Mean value		Mode		Coefficient of variation	
	Shell model	Solid model	Shell model	Solid model	Shell model	Solid model
E_x in Nm^{-2}	$1.13 \cdot 10^{10}$	$1.21 \cdot 10^{10}$	$1.13 \cdot 10^{10}$	$1.21 \cdot 10^{10}$	0.4%	0.4%
E_y in Nm^{-2}	$7.52 \cdot 10^{8}$	$2.73 \cdot 10^{8}$	$7.52 \cdot 10^{8}$	$2.73 \cdot 10^{8}$	0.3%	0.9%
G_{xy} in Nm^{-2}	$4.71 \cdot 10^{8}$	$4.65 \cdot 10^{8}$	$4.71 \cdot 10^{8}$	$4.65 \cdot 10^{8}$	0.5%	0.5%
ζ	$2.48 \cdot 10^{-2}$	$2.58 \cdot 10^{-2}$	$2.48 \cdot 10^{-2}$	$2.59 \cdot 10^{-2}$	3.2%	3.4%
σ_w	0.31	0.33	0.31	0.33	5.5%	4.8%
σ_θ	0.31	0.33	0.31	0.34	5.4%	4.6%
$l_{\mathrm{co},z}$ in m	49.8	49.6	47.5	50.8	17.8%	15.2%
$l_{\mathrm{co},f}$ in Hz	10.1	11.5	9.9	11.6	13.5%	10.7%
r	0.82	0.82	0.83	0.83	3.2%	2.7%

of the parameter r that controls the split between frequency and spatial domain correlation is shifted towards larger r around 0.8 for both models. From this we conclude that the model error behaves similarly for two response locations at a given frequency. However, for two distinct frequencies with $\Delta f \gg l_{\mathrm{co},f}$, the correlation of the model error at two response locations is around $1 - r \approx 0.2$, and thus low.

Fig. 5 shows that the joint posterior distribution of the solid model Young's moduli E_x and E_y exhibits significant correlation ($\rho = -0.74$). As the overall bending stiffness can be given by the weighted sum of the Young's moduli, a negative correlation as indicated in the second row and first column of the matrix in Fig. 5 is expected. With increasing E_x a decreasing E_y is necessary to obtain a similar overall bending stiffness and vice versa. Due to the homogenization of the material parameters for the shell model, this correlation is not observed in Fig. 4.

No significant correlation or dependence can be identified between the mechanical parameters and the hyperparameters of the error model. However, within the posterior hyperparameter samples, we make the following observations. The model error standard deviations for the log-absolute value and phase are positively correlated with correlation coefficient 0.66. This can be expected, as for larger errors in the absolute value it is plausible that also larger deviations in the phase occur and vice versa. Furthermore the frequency domain correlation length $l_{\mathrm{co},f}$ is positively correlated ($\rho \approx 0.8$) with both standard deviations of log-absolute value and phase. This indicates that whenever the deviation between model and measurement is large, these errors are similar over a larger range of frequencies. Additionally, a strong dependence can be observed between the factor r and σ_w, σ_θ as well as $l_{\mathrm{co},f}$. Large values of r correlate with large value of $l_{\mathrm{co},f}$ and vice versa. This indicates that for large errors the dependence among samples in the frequency domain is even larger than compared to smaller errors. The correlation structure among the hyperparameters is similar for the shell model.

The frequency response function evaluated at the mean of the posterior distribution is depicted in Fig. 6a. The mode shapes and eigenfrequencies of the solid model, based on the posterior mean values, are depicted in Fig. C.10 in Appendix C for completeness. We note that, based on the location of the amplitude peaks, the eigenfrequencies of the response are recovered quite well, whereas the amplitudes are not well predicted around the eigenfrequencies. As the attenuation in the vicinity of an eigenfrequency can be linked to the damping, we note a contradictory behavior. We would have to increase the damping ratio to explain the amplitude for some eigenfrequencies, whereas the damping ratio would have to be decreased to obtain the measured amplitude at the other eigenfrequencies. This cannot be achieved by a single damping ratio. Thus, we conclude that the applied damping model is too limited to capture the damping characteristics of the investigated CLT plate. Similar findings regarding the damping behavior of CLT plates were reported in [54]. Additionally to the measurement and model outcome based on the parameter means, Fig. 6 depicts the 95 % credible-intervals that are found from the posterior samples. We observe that the measurement is enclosed in the credible interval for almost all frequencies, except around the eigenfrequencies at around 90 and 105 Hz. Here, the deviation between measurement and model is very strong, which can again be linked to the damping model.

Estimates of the logarithm of the model evidence, as defined in Eq. (12), are 574.3 and 569.8 for the shell and

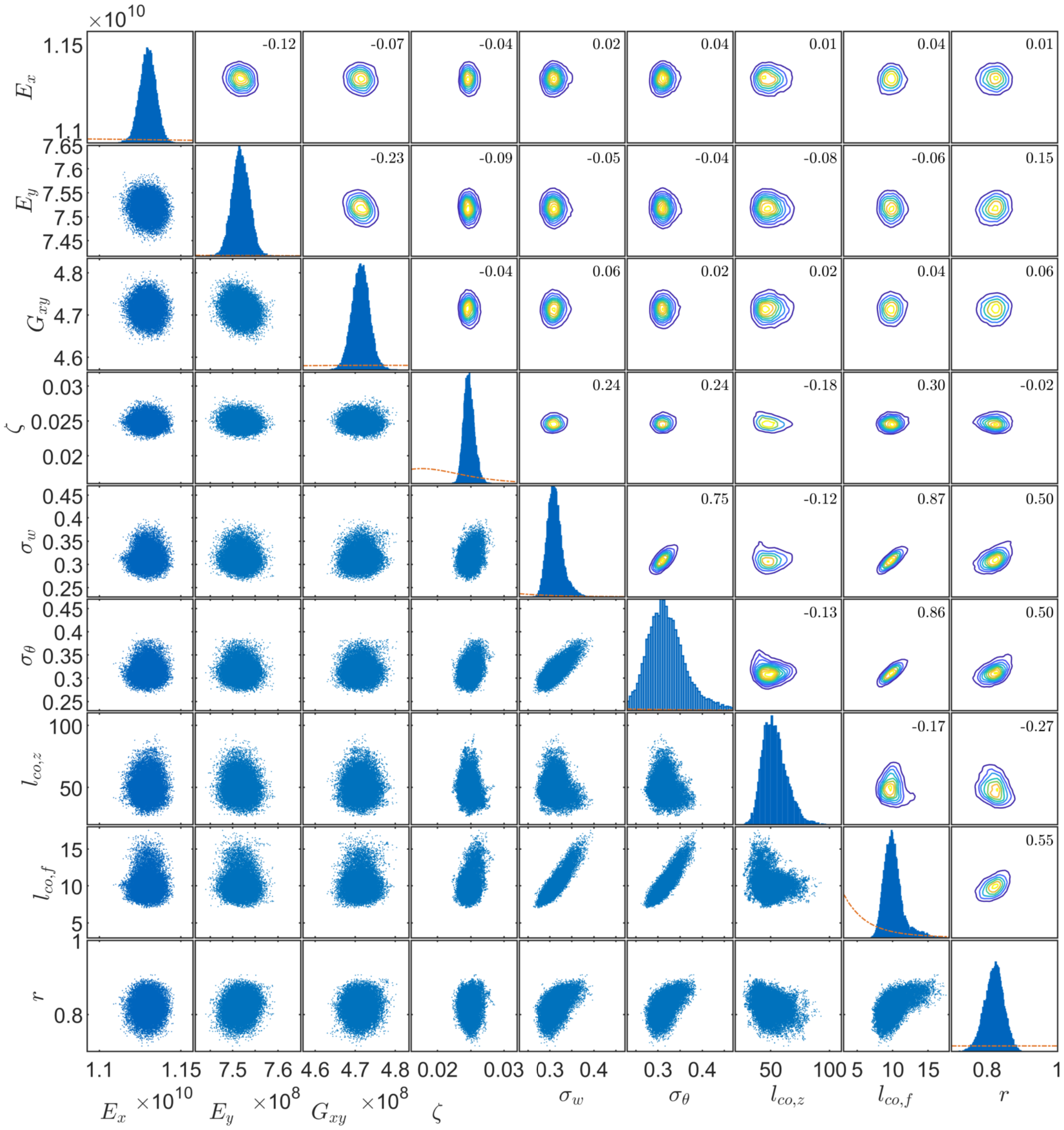

Figure 4: Posterior distribution for the shell model, described in terms of histograms of the posterior samples on the main diagonal (▮), bivariate scatter plots below the main diagonal (•), and bivariate density contour plots above the main diagonal (◎). The correlation coefficients are given in the top right corner of the density contour plots. Additionally, on the main diagonals, the marginal prior distributions (–·–) are given.

solid model, respectively, thus indicating a higher plausibility of the shell model. This is related to the identifiability of the models. As described above, for the solid model the correlation between the two Young's moduli is significant, such that the model is not as uniquely identifiable as compared to the shell model.

In what follows, we give resulting joint credible regions for the real and imaginary part of the real state of the structure with the shell model, based on the error model given in Eq. (13). Let $\tilde{H}_l$ be the frequency response of the

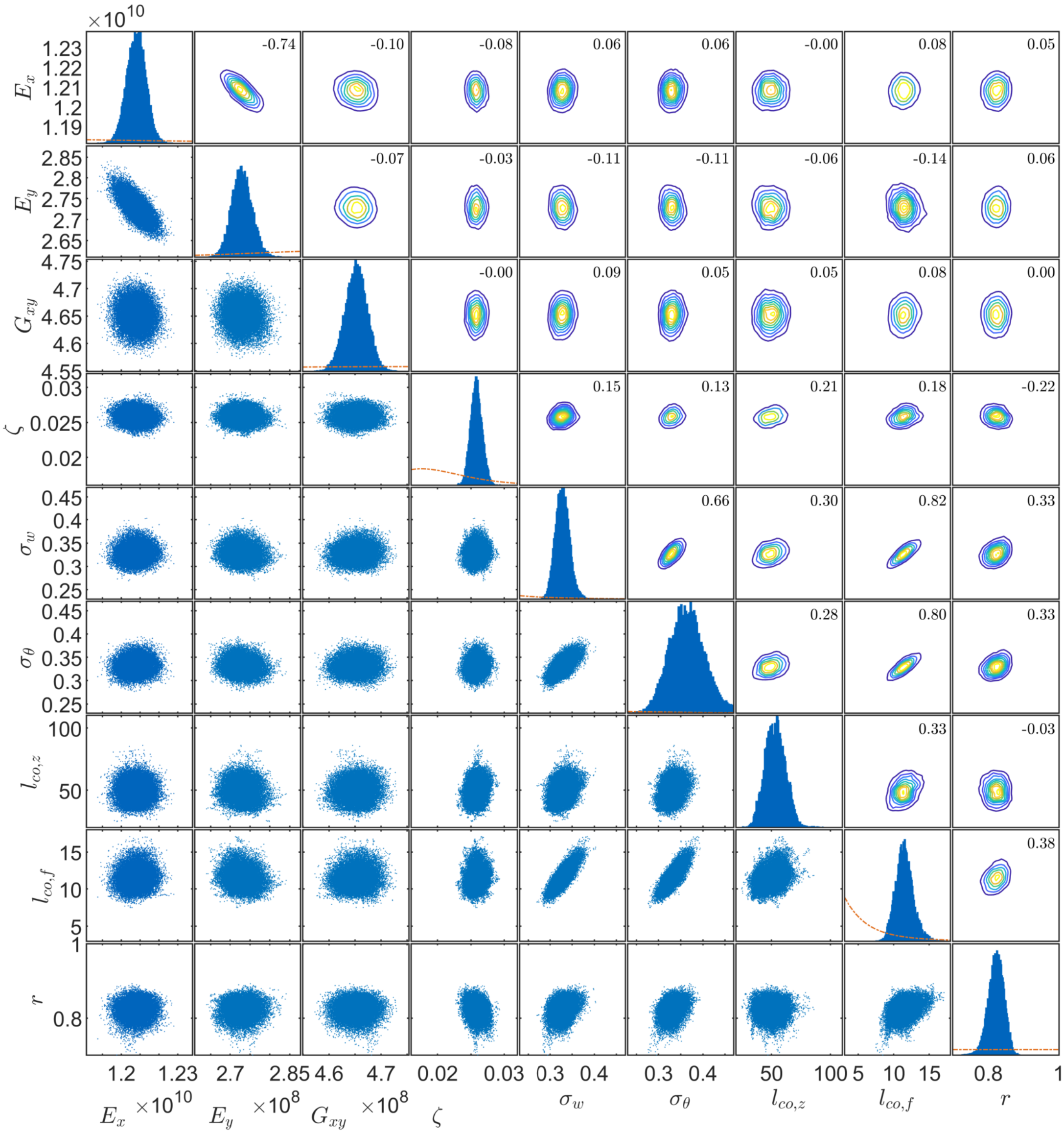

Figure 5: Posterior distribution for the solid model, described in terms of histograms of the posterior samples on the main diagonal (▮), bivariate scatter plots below the main diagonal (•), and bivariate density contour plots above the main diagonal (◎). The correlation coefficients are given in the top right corner of the density contour plots. Additionally, on the main diagonals, the marginal prior distributions (-·-) are given.

system at the l-th observation point. The credible regions are defined as the highest posterior density regions:

$$\int_{\tilde{H}_l : f_{\tilde{H}_l}(\tilde{h}_l|\mathcal{Y}_O) > f_{\alpha_l}} f_{\tilde{H}_l}(\tilde{h}_l|\mathcal{Y}_O)\,\mathrm{d}\tilde{h}_l = 1 - \alpha_l\,. \tag{31}$$

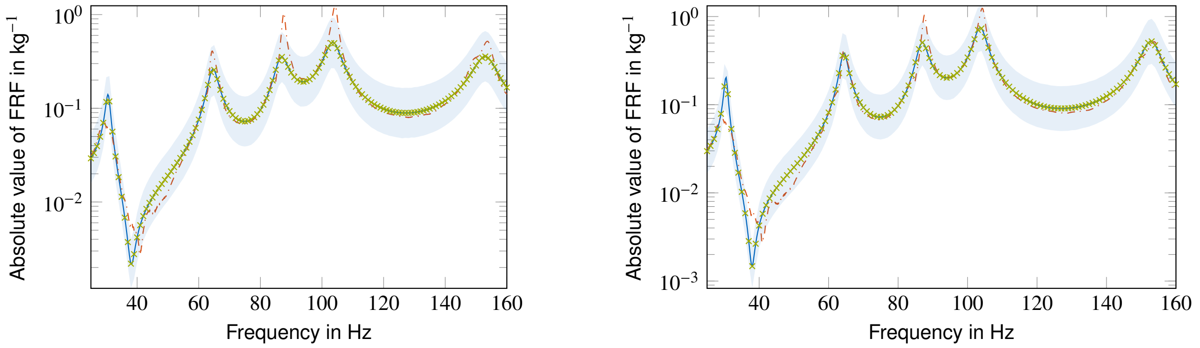

(a) Shell model, correlated model error

(b) Shell model, uncorrelated model error

Figure 6: Frequency response functions at location $i = 18$; (—) FRF with posterior mean values based on FE-model, (-·-) Measured FRF; (×) FRF with posterior mean values based on surrogate model. The blue shaded area ( ) indicates the 95 % credible interval.

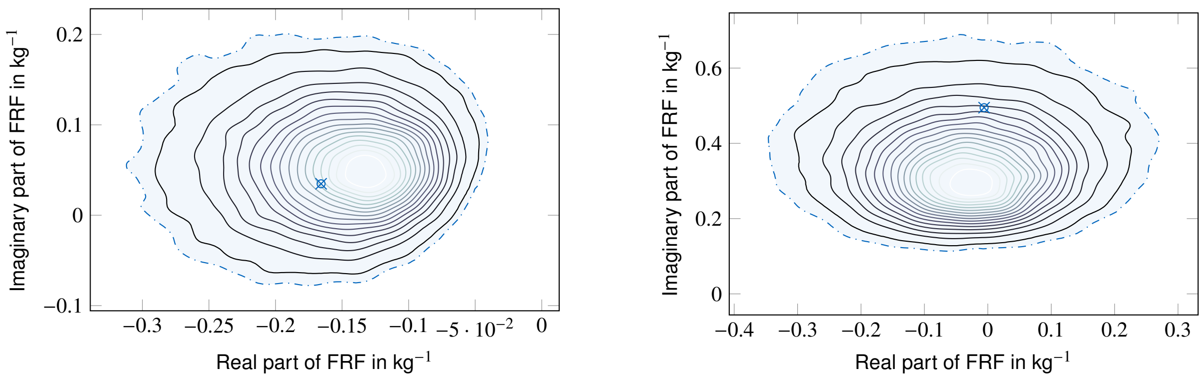

(a) $f = 145$ Hz, $i = 18$

(b) $f = 153$ Hz, $i = 18$

Figure 7: 95% credible region for the shell model. The solid iso-contours (◎) depict the joint PDF of real and imaginary part of the posterior predicted FRF. The shaded area ( ), bounded by the dash-dotted line, indicates the 95%-highest posterior density region. The blue marks (x) depict the actually observed value of the FRF resulting from the measurement.

Here, $\mathcal{Y}_O$ denotes the frequency transformed measurement data. Therefore, based on the posterior samples, we approximate the iso-contour $f_{\tilde{H}_l}(\tilde{h}_l|\mathcal{Y}_O) > f_{\alpha_l}$ that bounds $(1 - \alpha_l) \cdot 100\%$ of the posterior probability mass.

In Fig. 7 the resulting credible regions are depicted for spatial location $i = 18$ and frequencies $f \in \{145, 153\}$ Hz based on the shell model results. For $f = 145$ Hz (comp. Fig. 7a), the observation lies well within the credible area. Furthermore, the observation is close to the mode of the posterior predictive distribution. For $f = 153$ Hz (comp. Fig. 7b), the system is almost in resonance. This is indicated in the depicted posterior predictive distribution of the observed state as the average phase of the FRF is approximately $\frac{\pi}{2}$. The observed measurement lies well within the 95% credible region, however the amplitude is underestimated.

Out of all 680 observation points, in 611 cases the observation lies within the 95% credible region, i.e. in approximately 10% of the cases the observations lie outside of the 95% credible region. For the solid model, around 9 % of the observations lie outside of the 95% credible region. As discussed above, these points can be linked to the observations around the eigenfrequencies of the system. Furthermore, one can observe by comparison with Fig. 1c that the shape of the posterior predictive distribution of the real state of the structure is mainly governed by the model error (joint lognormal-normal model for absolute value and phase). One can interpret the resulting posterior predictive distribution approximately as a scaling and rotation of the joint model error PDF by the model prediction in the complex plane, since the overall uncertainty is mainly governed by the model error.

5.4.1. *Results under the Assumption of Uncorrelated Model Errors*

To investigate the effect of the correlation among the model errors, we compute posterior samples for the case without a model error correlation in the likelihood function. For this case, the hyperparameters linked to the correlation model are not considered. The posterior samples are shown in Figs. 8 for the shell model. Some noticeable differences are observed. Under this model, the posterior uncertainties, as reflected in the coefficients of variation (not shown here), reduce for all parameters. Furthermore, the identified damping values are significantly lower compared to the case with correlation in the model errors. Finally, the posterior standard deviations of the model errors do not show any correlation. It is worth mentioning that the different correlation assumptions mostly influence the posterior distribution of the damping parameter, while the estimates for the stiffness related parameters are similar to the case with error correlation.

The frequency response function evaluated at the mean of the posterior distribution for this case is depicted in Fig. 6b. We observe that due to the lower posterior uncertainty, the credible intervals are narrower compared to the result in Fig. 6a. Furthermore, due to the lower posterior mean value of the damping ratio ζ, the amplitudes in the FRF peaks are higher in comparison to the results obtained from the correlated case. When neglecting the correlation betweeen the model error for different observations, the mechanical model attempts to approximate the measurement more closely. This leads to lower identified damping values, which produce larger peak values in the FRF throughout the entire frequency range. While almost all peaks in the FRF are more closely captured in the uncorrelated case, the overestimation of the first peak around 30 Hz, which corresponds to the first torsional model shape, is larger than in the correlated case. In contrast, when considering the correlated error model, the deviations around the eigenfrequencies are better explained by the likelihood function and the identified damping value is large compared to to the uncorrelated case. Similar conclusions can be drawn for the solid model, but are omitted here for brevity.

6. Conclusion

This work presents a novel Bayesian updating procedure that utilizes frequency response function information, obtained from frequency transformed measurement data, directly. Bayesian updating is performed to infer the parameters of the mechanical model as well as the hyperparameters of the multiplicative error model. The likelihood formulation is derived in terms of the deviation between model outcome and measurement results in terms of the frequency response of the system. We propose a multivariate complex normal distribution for the logarithm of the model error, leading to a joint normal distribution for the logarithm of the absolute value and the phase of the model error. Furthermore an additive joint correlation model is chosen for the spatial and frequency domain, where we adopt exponential correlation functions and introduce a split-factor that models the share of the correlation in the two domains. Due to this correlation structure, the method is able to handle densely and uniformly sampled frequency domain data without further need to preselect or reduce the data. We use BUS with subset simulation to compute samples of the posterior distribution. To enhance the computational efficiency, we employ a recently introduced surrogate model that approximates the frequency response of the dynamic system through a rational of two polynomial chaos expansions with complex coefficients. These coefficients are determined with a non-intrusive regression-based approach.

The method is successfully applied to learn the parameters of the mechanical model of a cross-laminated timber plate with frequency transformed measurements. We investigate two different mechanical models, one shell and one solid model. For both models a subset of the full orthotropic material parameter set is identified, where for the shell model the material parameters describe an equivalent homogeneous material. The damping behavior of the structure is modeled by global linear hysteretic damping. The results show that the uncertainty on the mechanical parameters can be significantly reduced. It is shown that for the given models we obtain a large model error standard deviation, which can be linked to the chosen linear hysteretic damping model. For the given structure the damping characteristics are not modeled well by this damping model. The resulting amplitudes in the frequency response function can thus not be well explained through a single damping coefficient. We further show that the assumption of correlated samples has a noticeable effect on the resulting posterior distributions. Whereas the estimates of the stiffness related terms are similar, the estimates of the damping term as well as the model error standard deviations are influenced by the correlation model choice.

Further research could aim at investigating the performance of the method for measurements that use different excitation techniques and accelerometers, e.g. [19, 4]. A side benefit could be a better understanding of the non-

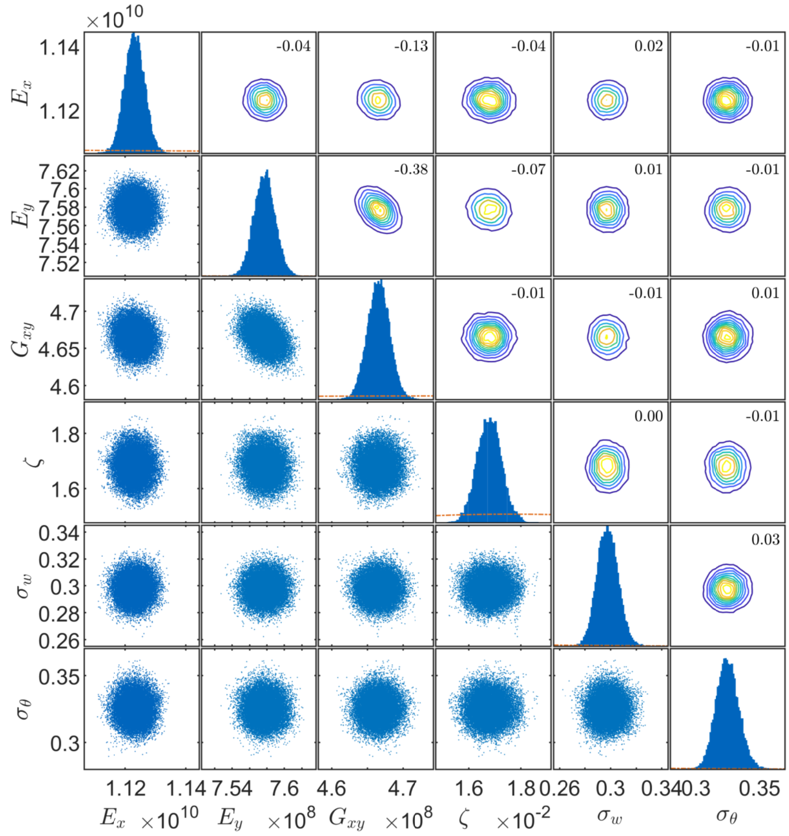

Figure 8: Posterior distribution for the shell model, when assuming uncorrelated model errors, described in terms of histograms of the posterior samples on the main diagonal (▮), bivariate scatter plots below the main diagonal (•), and bivariate density contour plots above the main diagonal (◎). The correlation coefficients are given in the top right corner of the density contour plots. Additionally, on the main diagonals, the marginal prior distributions (–·–) are given.

linearities in the systems under investigation. Additionally, the results could be compared to a modal analysis based approach. The authors are furthermore working on the influence of different correlation function assumptions and more detailed mechanical models of the structure. Finally, an extension of the considered frequency range is of interest.

Acknowledgement

The authors thank Max Ehre for his helpful comments and insightful discussions. This work was supported by the Deutsche Forschungsgemeinschaft (DFG) in the framework of the priority program SPP by grant STR 1140/6-1

Appendix A. Joint PDF of real and imaginary part of the model error

In order to derive the joint PDF of the real and imaginary part of the model error $\boldsymbol{\varepsilon}$, for the sake of clarity, we repeat the definitions of the relevant quantities. In the following we denote by $\mathbf{w} = \log|\boldsymbol{\varepsilon}|$ the logarithm of the absolute value of the model error, by $\boldsymbol{\theta} = \arg \boldsymbol{\varepsilon}$ the phase of the model error, by $\mathbf{u} = \mathrm{Re}\{\boldsymbol{\varepsilon}\}$ the real part of the model error and by $\mathbf{v} = \mathrm{Im}\{\boldsymbol{\varepsilon}\}$ the imaginary part of the model error. From these quantities we derive the real composite vectors

$\mathbf{z} = [\mathbf{u}; \mathbf{v}]$ and $\boldsymbol{\xi} = [\mathbf{w}; \boldsymbol{\theta}]$ The joint distribution of the real and imaginary part of the model error can then be computed by

$$f_{\mathbf{Z}}(\mathbf{z}) = f_{\xi}\left(\mathbf{T}^{-1}(\mathbf{z})\right)\left|\det\left(\mathbf{J}_{\xi,\mathbf{z}}\right)\right| . \tag{A.1}$$

Here, $f_{\xi}(\boldsymbol{\xi})$ denotes the joint PDF of $\mathbf{w}$ and $\boldsymbol{\theta}$. Recall that we assume this distribution to be a zero-mean Gaussian distribution, i.e.:

$$f_{\xi}(\boldsymbol{\xi}) = \frac{1}{(2\pi)^{\frac{n_O}{2}}\sqrt{\det \mathbf{R}_{\mathbf{ww}}}} \exp\left\{-\frac{1}{2}\mathbf{w}^T R_{\mathbf{ww}}^{-1}\mathbf{w}\right\} \times \frac{1}{(2\pi)^{\frac{n_O}{2}}\sqrt{\det \mathbf{R}_{\theta\theta}}} \exp\left\{-\frac{1}{2}\boldsymbol{\theta}^T R_{\theta\theta}^{-1}\boldsymbol{\theta}\right\} . \tag{A.2}$$

The transformation $\mathbf{T} : \mathbb{R}^{2n_O} \to \mathbb{R}^{2n_O}$ is defined as

$$\mathbf{z} = \begin{pmatrix}\mathbf{u}\\ \mathbf{v}\end{pmatrix} = \mathbf{T}(\boldsymbol{\xi}) = \begin{pmatrix}\exp\{\mathbf{w}\}\cos(\boldsymbol{\theta})\\ \exp\{\mathbf{w}\}\sin(\boldsymbol{\theta}) .\end{pmatrix} . \tag{A.3}$$

from which we find the inverse transformation $\mathbf{T}^{-1} : \mathbb{R}^{2n_O} \to \mathbb{R}^{2n_O}$:

$$\boldsymbol{\xi} = \begin{pmatrix}\mathbf{w}\\ \boldsymbol{\theta}\end{pmatrix} = \mathbf{T}^{-1}(\mathbf{z}) = \begin{pmatrix}\log\sqrt{\mathbf{u}^{\circ 2} + \mathbf{v}^{\circ 2}}\\ \operatorname{atan2}(\mathbf{v}, \mathbf{u})\end{pmatrix} . \tag{A.4}$$

where atan2 is an extension of the inverse tangent function that yields the angle of a complex number in the complex plane in the range $]-\pi, \pi]$. $\mathbf{J}_{\xi,\mathbf{z}}$ denotes the Jacobian matrix of the transformation, defined as:

$$\mathbf{J}_{\xi,\mathbf{z}} = \left[\frac{\partial \xi_i}{\partial z_j}\right]_{2n_O \times 2n_O} . \tag{A.5}$$

In order to evaluate the determinant of the Jacobian matrix, we use the identity $\det\left(\mathbf{J}_{\xi,\mathbf{z}}\right) = \frac{1}{\det\left(\mathbf{J}_{\mathbf{z},\xi}\right)}$ and find:

$$\det\left(\mathbf{J}_{\mathbf{z},\xi}\right) = \det\begin{bmatrix}
\mathrm{e}^{w_1}\cos(\theta_1) & 0 & \dots & 0 & -\mathrm{e}^{w_1}\sin(\theta_1) & 0 & \dots & 0\\
0 & \mathrm{e}^{w_2}\cos(\theta_2) & \dots & 0 & 0 & -\mathrm{e}^{w_2}\sin(\theta_2) & \dots & 0\\
\vdots & \vdots & \ddots & \vdots & \vdots & \vdots & \ddots & \vdots\\
0 & 0 & \dots & \mathrm{e}^{w_{n_O}}\cos(\theta_{n_O}) & 0 & 0 & \dots & -\mathrm{e}^{w_{n_O}}\sin(\theta_{n_O})\\
\mathrm{e}^{w_1}\sin(\theta_1) & 0 & \dots & 0 & \mathrm{e}^{w_{n_1}}\cos(\theta_1) & 0 & \dots & 0\\
0 & \mathrm{e}^{w_2}\sin(\theta_2) & \dots & 0 & 0 & \mathrm{e}^{w_{n_2}}\cos(\theta_2) & \dots & 0\\
\vdots & \vdots & \ddots & \vdots & \vdots & \vdots & \ddots & \vdots\\
0 & 0 & \dots & \mathrm{e}^{w_{n_O}}\sin(\theta_{n_O}) & 0 & 0 & \dots & \mathrm{e}^{w_{n_O}}\cos(\theta_{n_O})
\end{bmatrix} . \tag{A.6}$$

We rearrange the columns and rows of the Jacobian matrix and obtain:

$$\det\left(\mathbf{J}_{\mathbf{z},\xi}\right) = \det\begin{bmatrix}
\mathrm{e}^{w_1}\cos(\theta_1) & -\mathrm{e}^{w_1}\sin(\theta_1) & 0 & 0 & \dots & 0 & 0\\
\mathrm{e}^{w_1}\sin(\theta_1) & \mathrm{e}^{w_1}\cos(\theta_1) & 0 & 0 & \dots & 0 & 0\\
0 & 0 & \mathrm{e}^{w_2}\cos(\theta_2) & -\mathrm{e}^{w_2}\sin(\theta_2) & \dots & 0 & 0\\
0 & 0 & \mathrm{e}^{w_2}\sin(\theta_2) & \mathrm{e}^{w_2}\cos(\theta_2) & \dots & 0 & 0\\
\vdots & \vdots & \vdots & \vdots & \ddots & \vdots & \vdots\\
0 & 0 & 0 & 0 & \dots & \mathrm{e}^{w_{n_O}}\cos(\theta_{n_O}) & -\mathrm{e}^{w_{n_O}}\sin(\theta_{n_O})\\
0 & 0 & 0 & 0 & \dots & \mathrm{e}^{w_{n_O}}\sin(\theta_{n_O}) & \mathrm{e}^{w_{n_O}}\cos(\theta_{n_O})
\end{bmatrix} . \tag{A.7}$$

Swapping a column or row leads to a multiplication of the determinant by -1. The above rearrangement will result in an even number of swapping operations, thus the sign of the determinant will stay unchanged and the equality still holds. Since the matrix in the above equation is block-diagonal, we find its determinant as the product of the determinant of the n_O 2×2 submatrices:

$$\det\left(\mathbf{J}_{\mathbf{z},\xi}\right) = \prod_{i=1}^{n_O} (\mathrm{e}^{w_1})^2 \left(\cos^2(\theta_i) + \sin^2(\theta_i)\right) = \prod_{i=1}^{n_O} \mathrm{e}^{w_1^2} = \prod_{i=1}^{n_O} \left(u_i^2 + v_i^2\right) . \tag{A.8}$$

Inserting Eqs. (A.2), (A.4) and the inverse of (A.8) into Eq. (A.1), we finally obtain the joint PDF of the real and imaginary parts of the model error:

$$f_{\mathbf{Z}}(\mathbf{z}) = \frac{1}{(2\pi)^{n_O} \det\left(\operatorname{diag}\left(\mathbf{u}^{\circ 2} + \mathbf{v}^{\circ 2}\right)\right) \sqrt{\det \mathbf{R}_{\mathbf{ww}} \det \mathbf{R}_{\theta\theta}}} \exp\left\{-\frac{1}{2} \log\left(\mathbf{u}^{\circ 2} + \mathbf{v}^{\circ 2}\right)^T \mathbf{R}_{\mathbf{ww}}^{-1} \log\left(\mathbf{u}^{\circ 2} + \mathbf{v}^{\circ 2}\right)\right\} \times$$
$$\times \exp\left\{-\frac{1}{2} \left(\operatorname{atan2}(\mathbf{v}, \mathbf{u})\right)^T \mathbf{R}_{\theta\theta}^{-1} \left(\operatorname{atan2}(\mathbf{v}, \mathbf{u})\right)\right\}. \quad \text{(A.9)}$$

It should be noted that this PDF is not defined for any u_i or v_i equal to zero.

Appendix B. Error measures

In order to evaluate the accuracy of the surrogate models, we consider the cross validation error, as defined in [41]. Therefore, the experimental design $\mathcal{X}$ is partitioned into n_{cv} subsets $\{\mathcal{X}_1, \ldots, \mathcal{X}_{n_{\mathrm{cv}}}\}$ of equal size, called the test sets. n_{cv} surrogate models $\hat{\mathcal{M}}_{\setminus i}$ are built, each based on the reduced experimental designs $\{\mathcal{X}_1, \ldots, \mathcal{X}_{n_{\mathrm{cv}}}\} \setminus \{\mathcal{X}_i\}$, $i = 1, \ldots, n_{\mathrm{cv}}$, called the training sets. For each i, the squared error at the points in $\{\mathcal{X}_i\}$ is evaluated. The jth element in subset $\{\mathcal{X}_i\}$ is denoted by x_i^j. The cross validation error is then defined by the sum of the squared predicted residuals and is calculated as

$$\mathrm{err}_{\mathrm{cv}} = \sum_{i=1}^{n_{\mathrm{cv}}} \sum_{j=1}^{\operatorname{card}(\mathcal{X}_i)} \left(\mathcal{M}\left(x_i^j\right) - \hat{\mathcal{M}}_{\setminus i}\left(x_i^j\right)\right)^2, \quad \text{(B.1)}$$

where $\operatorname{card}(\cdot)$ denotes the cardinality of a set. A relative version of the above error can be defined using the empirical variance.

$$\varepsilon_{\mathrm{cv}} = \frac{\mathrm{err}_{\mathrm{cv}}}{\widehat{\mathrm{Var}}\left[\mathcal{M}(x)\right]}. \quad \text{(B.2)}$$

We use $N = 4$, i.e. the 4-fold cross validation error.

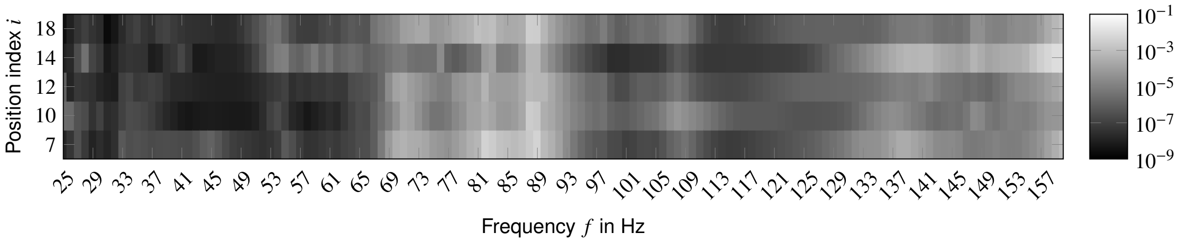

(a) Shell model

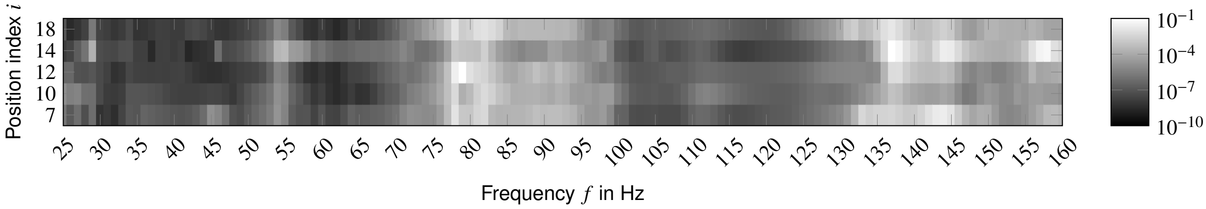

(b) Solid model

Figure B.9: Relative 4-fold cross-validation error for surrogate models.

Appendix C. Mode shapes of the shell model

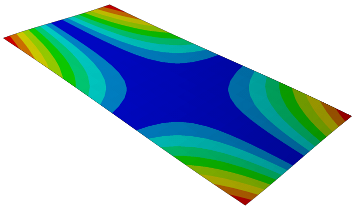

(a) Mode 1, $f_1 = 30.8\,\mathrm{Hz}$

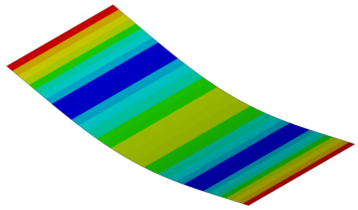

(b) Mode 2, $f_2 = 64.7\,\mathrm{Hz}$

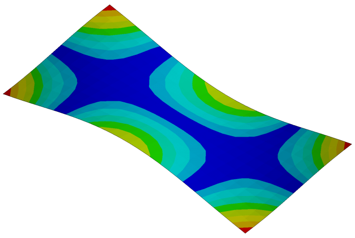

(c) Mode 3, $f_3 = 87.0\,\mathrm{Hz}$

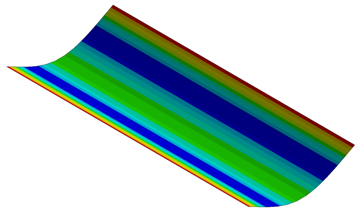

(d) Mode 4, $f_4 = 87.7\,\mathrm{Hz}$

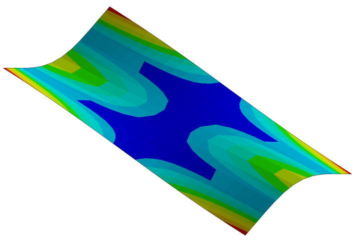

(e) Mode 5, $f_5 = 105.0\,\mathrm{Hz}$

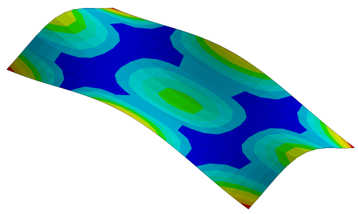

(f) Mode 6, $f_6 = 155.0\,\mathrm{Hz}$

Figure C.10: Mode shapes for the shell model and corresponding eigenfrequencies, based on posterior mean values.

References

[1] K. J. Åström, P. Eykhoff, System identification—A survey, Automatica 7 (1971) 123–162.

[2] T. Soederstroem, P. Stoica, System Identification, Prentice Hall International Series in Systems and Control Engineering, Prentice Hall, New York and London, 1989.

[3] J. E. Mottershead, M. I. Friswell, Model updating in structural dynamics: A survey, Journal of Sound and Vibration 167 (1993) 347–375.

[4] R. Pintelon, J. Schoukens, System identification: a frequency domain approach, John Wiley & Sons, 2012.

[5] H. G. Natke (Ed.), Identification of Vibrating Structures, Springer, 1982.

[6] E. Simoen, G. Lombaert, Bayesian parameter estimation, in: Identification Methods for Structural Health Monitoring, Springer, 2016, pp. 89–115.

[7] M. Friswell, J. E. Mottershead, Finite element model updating in structural dynamics, volume 38, Springer Science & Business Media, 2013.

[8] A. Gelman, H. S. Stern, J. B. Carlin, D. B. Dunson, A. Vehtari, D. B. Rubin, Bayesian data analysis, Chapman and Hall/CRC, 2013.

[9] V. Peterka, Bayesian approach to system identification, in: Trends and Progress in System Identification, Elsevier, 1981, pp. 239–304.

[10] J. L. Beck, L. S. Katafygiotis, Updating models and their uncertainties. I: Bayesian statistical framework, Journal of Engineering Mechanics 124 (1998) 455–461.

[11] K.-V. Yuen, Bayesian methods for structural dynamics and civil engineering, John Wiley & Sons, 2010.

[12] D. J. MacKay, D. J. Mac Kay, Information theory, inference and learning algorithms, Cambridge University Press, 2003.

[13] W. R. Gilks, S. Richardson, D. Spiegelhalter, Markov chain Monte Carlo in practice, Chapman and Hall/CRC, 1995.

[14] J. L. Beck, S.-K. Au, Bayesian updating of structural models and reliability using markov chain monte carlo simulation, Journal of Engineering Mechanics 128 (2002) 380–391.

[15] S. H. Cheung, S. Bansal, A new gibbs sampling based algorithm for bayesian model updating with incomplete complex modal data, Mechanical Systems and Signal Processing 92 (2017) 156–172.

[16] M. Muto, J. L. Beck, Bayesian updating and model class selection for hysteretic structural models using stochastic simulation, Journal of Vibration and Control 14 (2008) 7–34.

[17] J. L. Beck, Bayesian system identification based on probability logic, Structural Control and Health Monitoring 17 (2010) 825–847.

[18] E. Zhang, P. Feissel, J. Antoni, Bayesian model updating with consideration of modeling error, European Journal of Computational Mechanics 19 (2010) 255–266.

[19] E. L. Zhang, P. Feissel, J. Antoni, A comprehensive bayesian approach for model updating and quantification of modeling errors, Probabilistic Engineering Mechanics 26 (2011) 550–560.

[20] E. Zhang, J. D. Chazot, J. Antoni, M. Hamdi, Bayesian characterization of young's modulus of viscoelastic materials in laminated structures, Journal of Sound and Vibration 332 (2013) 3654–3666.

[21] D. Straub, I. Papaioannou, Bayesian updating with structural reliability methods, Journal of Engineering Mechanics 141 (2015) 04014134.

[22] F. DiazDelaO, A. Garbuno-Inigo, S. Au, I. Yoshida, Bayesian updating and model class selection with subset simulation, Computer Methods in Applied Mechanics and Engineering 317 (2017) 1102–1121.

[23] W. Betz, I. Papaioannou, J. L. Beck, D. Straub, Bayesian inference with subset simulation: Strategies and improvements, Computer Methods in Applied Mechanics and Engineering 331 (2018) 72–93.

[24] R. G. Ghanem, P. D. Spanos, Stochastic finite element method: Response statistics, in: Stochastic Finite Elements: A Spectral Approach, Springer, 1991, pp. 101–119.

[25] D. Xiu, G. E. Karniadakis, The Wiener–Askey polynomial chaos for stochastic differential equations, SIAM Journal on Scientific Computing 24 (2002) 619–644.

[26] F. Yamazaki, M. Shinozuka, G. Dasgupta, Neumann expansion for stochastic finite element analysis, Journal of Engineering Mechanics 114 (1988) 1335–1354.

[27] M. Papadrakakis, V. Papadopoulos, N. D. Lagaros, Structural reliability analyis of elastic-plastic structures using neural networks and Monte Carlo simulation, Computer Methods in Applied Mechanics and Engineering 136 (1996) 145–163.

[28] C. E. Rasmussen, C. K. I. Williams, Gaussian processes for machine learning, Adaptive computation and machine learning, MIT Press, Cambridge, Mass., 3. print edition, 2008.

[29] P. Angelikopoulos, C. Papadimitriou, P. Koumoutsakos, X-TMCMC: Adaptive kriging for Bayesian inverse modeling, Computer Methods in Applied Mechanics and Engineering 289 (2015) 409–428.

[30] D. G. Giovanis, I. Papaioannou, D. Straub, V. Papadopoulos, Bayesian updating with subset simulation using artificial neural networks, Computer Methods in Applied Mechanics and Engineering 319 (2017) 124–145.

[31] S. Au, F. Zhang, Field measurement and bayesian modal identification of a primary-secondary structure, Procedia Engineering 14 (2011) 2593–2600.

[32] H.-F. Lam, J. Yang, S.-K. Au, Bayesian model updating of a coupled-slab system using field test data utilizing an enhanced markov chain monte carlo simulation algorithm, Engineering Structures 102 (2015) 144–155.

[33] T. Marwala, S. Sibisi, Finite element model updating using bayesian framework and modal properties, Journal of Aircraft 42 (2005) 275–278.

[34] K. Sepahvand, S. Marburg, Non-sampling inverse stochastic numerical–experimental identification of random elastic material parameters in composite plates, Mechanical Systems and Signal Processing 54 (2015) 172–181.

[35] J.-N. Juang, R. S. Pappa, An eigensystem realization algorithm for modal parameter identification and model reduction, Journal of Guidance, Control, and Dynamics 8 (1985) 620–627.

[36] W. Heylen, S. Lammens, P. Sas, Modal analysis theory and testing, Katholieke Univ. Leuven, Departement Werktuigkunde, Leuven, 2013.

[37] P. Guillaume, P. Verboven, S. Vanlanduit, H. van der Auweraer, B. Peeters, A poly-reference implementation of the least-squares complex frequency-domain estimator, Proceedings of IMAC 21 (2003).

[38] M. Imregun, W. J. Visser, D. J. Ewins, Finite element model updating using frequency response function data, Mechanical Systems and Signal Processing 9 (1995) 187–202.

[39] C. Mares, B. Dratz, J. Mottershead, M. Friswell, Model updating using Bayesian estimation, in: International Conference on Noise and Vibration Engineering, ISMA2006, Katholieke Universiteit Leuven, pp. 18–20.

[40] C. Soize, Bayesian posteriors of uncertainty quantification in computational structural dynamics for low-and medium-frequency ranges, Computers & Structures 126 (2013) 41–55.

[41] F. Schneider, I. Papaioannou, M. Ehre, D. Straub, Polynomial chaos based rational approximation in linear structural dynamics with parameter uncertainties, Computers & Structures 233 (2020) 106223.

[42] R. G. Ghanem, P. D. Spanos, Stochastic Finite Elements: A Spectral Approach, Springer New York, New York, NY, 1991.

[43] Jacquelin E., Dessombz O., Sinou J.–J., Adhikari S., Friswell M. I., Polynomial chaos–based extended padé expansion in structural dynamics, International Journal for Numerical Methods in Engineering 111 (2016) 1170–1191.

[44] M. Rosenblatt, Remarks on a multivariate transformation, The Annals of Mathematical Statistics 23 (1952) 470–472.

[45] J. L. Beck, K.-V. Yuen, Model selection using response measurements: Bayesian probabilistic approach, Journal of Engineering Mechanics 130 (2004) 192–203.

[46] P. J. Schreier, L. L. Scharf, Statistical signal processing of complex-valued data: The theory of improper and noncircular signals, Cambridge University Press, Cambridge, 2010.

[47] E. Simoen, C. Papadimitriou, G. Lombaert, On prediction error correlation in bayesian model updating, Journal of Sound and Vibration 332 (2013) 4136–4152.

[48] S.-K. Au, J. L. Beck, Estimation of small failure probabilities in high dimensions by subset simulation, Probabilistic Engineering Mechanics 16 (2001) 263–277.

[49] I. Papaioannou, W. Betz, K. Zwirglmaier, D. Straub, MCMC algorithms for subset simulation, Probabilistic Engineering Mechanics 41 (2015) 89–103.

[50] R. Brandner, G. Flatscher, A. Ringhofer, G. Schickhofer, A. Thiel, Cross laminated timber (CLT): overview and development, European Journal of Wood and Wood Products 74 (2016) 331–351.

[51] B. van Damme, S. Schoenwald, A. Zemp, Modeling the bending vibration of cross-laminated timber beams, European Journal of Wood and Wood Products 75 (2017) 985–994.

[52] J. Bodig, B. A. Jayne, Mechanics of wood and wood composites, volume 712, Van Nostrand Reinhold New York, 1982.

[53] ANSYS® Academic Research Mechanical, 2017.

[54] N. Labonnote, Damping in timber structures, Dissertation, 2012.

[55] S. Mecking, T. Kruse, C. Winter, U. Schanda, Schlussbericht: Vibroakustik im Planungsprozess für Holzbauten: Teilprojekt 3: Parameterentwicklung und SEA-Modellierung: Research Report, 2017.

[56] E. Oran Brigham, The fast fourier transform and its applications, UK: Prentice Hall (1988).

[57] C. Winter, Frequency Dependent Modeling for the Prediction of the Sound Transmission in Timber Constructions, Dissertation, Technical University of Munich, 2018.

[58] DIN Deutsches Institut für Normung e. V., Structural timber - strength classes, 2016.

[59] J. JCSS, Probabilistic model code, Joint Committee on Structural Safety (2001).

[60] A. Paolini, S. Kollmannsberger, C. Winter, M. Buchschmid, G. Müller, A. Rabold, S. Mecking, U. Schanda, E. Rank, A high-order finite element model for vibration analysis of cross-laminated timber assemblies, Building Acoustics 24 (2017) 135–158.